

Electronic and magnetic structures of a mixed triple perovskite: Ba₃NiRuIrO₉

Siddharth Kumar^{1,*}, Kuldeep Kargeti,² D. C. Joshi³, Gangadhar Das^{4,5}, Ranjan Kumar Patel^{1,†}, John W. Freeland⁶, Luca Olivi⁵, Giuliana Aquilanti,⁵ S. D. Kaushik⁷, Roland Mathieu³, S. K. Panda,^{2,‡} D. D. Khalyavin,⁸ and Srimanta Middey^{1,§}

¹*Department of Physics, Indian Institute of Science, Bengaluru 560012, India*

²*Department of Physics, Bennett University, Greater Noida, Uttar Pradesh 201310, India*

³*Department of Materials Science and Engineering, Uppsala University, Box 35, 751 03 Uppsala, Sweden*

⁴*Chemistry and Physics of Materials Unit, Jawaharlal Nehru Centre for Advanced Scientific Research, Jakkur, Bengaluru 560064, India*

⁵*Elettra–Sincrotrone Trieste, s.s. 14 - km 163, 5 in AREA Science Park, 34149 Basovizza, Trieste, Italy*

⁶*Advanced Photon Source, Argonne National Laboratory, Argonne, Illinois 60439, USA*

⁷*UGC-DAE Consortium for Scientific Research Mumbai Centre, R-5 Shed, BARC, Mumbai 400085, India*

⁸*ISIS Facility, STFC Rutherford Appleton Laboratory, Didcot, Oxfordshire OX11 0QX, United Kingdom*



(Received 4 March 2024; revised 10 June 2024; accepted 11 June 2024; published 8 July 2024)

In search of spin-orbit coupling driven nonmagnetic $J = 0$ ground state and excitonic magnetism, various pentavalent iridates have been studied in recent years. However, a finite moment was observed in most of the cases due to solid state effects. In this work, we investigate the electronic and magnetic structure of $6H$ hexagonal compound Ba₃NiRuIrO₉, where Ir⁵⁺ is present along with magnetic Ni²⁺ and Ru⁵⁺ ions. Magnetic susceptibility measurements and neutron powder diffraction (NPD) experiments demonstrate the appearance of short-range magnetic ordering below 170 K and a long-range antiferromagnetic ordering below 80 K. The refinement of the NPD pattern further shows that the Ru and Ir moments interact antiferromagnetically within the dimer and interact ferromagnetically with the Ni sublattice. These experimental findings have been complemented by first-principles density functional theory calculations incorporating spin-orbit coupling effects and electronic correlations for the transitional metal d states. The computed magnetocrystalline anisotropy is also found to be significant and the crystallographic c axis comes out to be the easy axis of magnetization, consistent with the spin alignment direction found from NPD. This study shows that the mixed ruthenate iridate triple perovskite series is a promising family to study the interplay among spin-orbit coupling, electron correlation, and electron filling as a variety of Ba₃MRuIrO₉ with M as a transition metal ion, rare-earth ion, and alkali metal ions can be synthesized.

DOI: [10.1103/PhysRevB.110.024407](https://doi.org/10.1103/PhysRevB.110.024407)

I. INTRODUCTION

Transition metal oxides (TMOs) with $3d$ elements of the Periodic Table are hosts of a variety of tunable electronic and magnetic phenomena due to the strong intercoupling amongst spin, charge, lattice, and orbital degrees of freedom [1]. In traversing from $3d \rightarrow 4d \rightarrow 5d$ TMOs, the d orbital becomes spatially more extended, resulting in a higher crystal field (CF) splitting and lower effective electron correlation (U/W) (U and W denote electron correlation and hybridization strength between TM d and O p states, respectively). On the other hand, the spin-orbit coupling (SOC) strength, which is generally negligible for $3d$ TMOs, becomes a decisive

energy scale in $4d/5d$ TMOs [2–6]. For example, $3d$ TMOs with d^4 electronic configuration in octahedral crystal field generally have a high spin state with $S = 2$ (e.g., LaMnO₃) [7]. In sharp contrast, strong SOC in $4d/5d$ oxides would lead to a nonmagnetic $J = 0$ state for t_{2g}^4 configuration [Fig. 1(a)] and the magnetic response would be governed by singlet to triplet excitation [8]. The possibility of such excitonic magnetism has prompted extensive attempts in recent years to stabilize the Ir⁵⁺ ion within diverse structural networks such as cubic [9], hexagonal [10–12], double perovskite [13–15], postperovskite [16], and pyrochlore [17,18] arrangements (see Ref. [19] for review). However, in many cases, a finite moment at the Ir site was observed, which has been attributed to various solid state effects such as hybridization, noncubic crystal field, disorder, etc. [20,21].

In search of an SOC driven nonmagnetic $J = 0$ state, several Ba₃MIr₂O₉ compounds with nonmagnetic M^{2+} ($M = \text{Sr, Ca, Mg, Zn, Cd}$) have been investigated over the last several years [10,11,22]. Here, the IrO₆ unit forms face-sharing dimers, which are connected to the MO₆ octahedra through corner-sharing oxygen [see Fig. 1(b)], forming a buckled honeycomb lattice [Fig. 1(c)]. The dimers also form a triangular

*Present address: Department of Electrical and Computer Engineering, Rutgers University, Piscataway, NJ 08854, USA; Contact author: siddharthk@iisc.ac.in

†Present address: Department of Electrical and Computer Engineering, Rutgers University, Piscataway, NJ 08854, USA.

‡Contact author: swarup.panda@bennett.edu.in

§Contact author: smiddey@iisc.ac.in

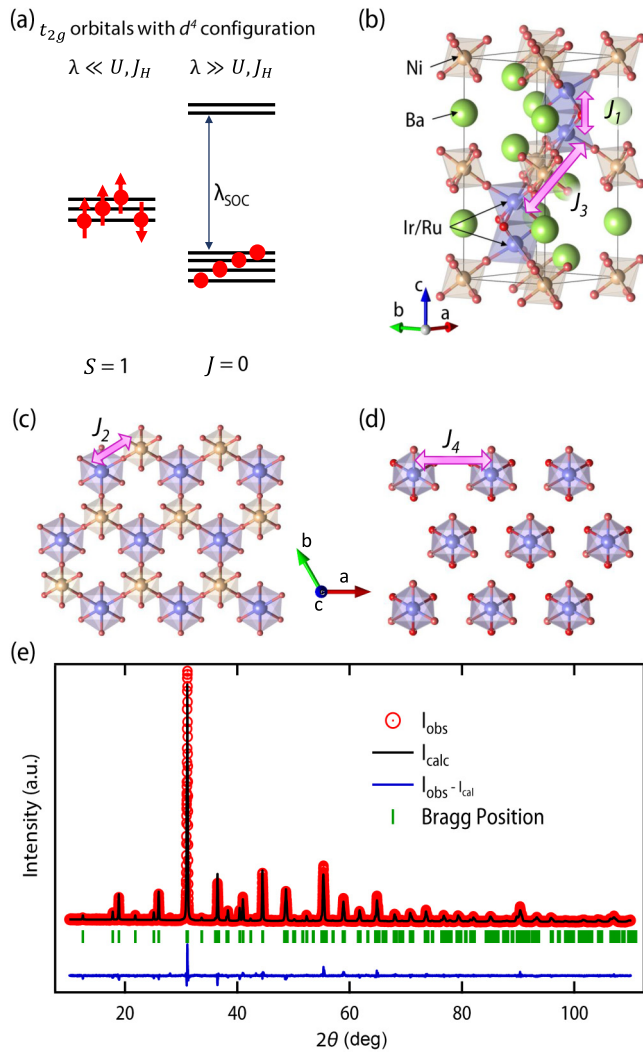


FIG. 1. (a) Splitting of t_{2g} with d^4 configuration with and without SOC. J_H and λ denote Hund's coupling and SOC strength, respectively. The energy gaps are not according to the scale. (b) Unit cell of $\text{Ba}_3\text{NiRuIrO}_9$ showing the position of different atoms. (c) The Ru/Ir-O-Ni connectivity forms a buckled honeycomb lattice. (d) $(\text{Ru/Ir})_2\text{O}_9$ dimers are arranged in a triangular way in the $a - b$ plane. Different magnetic exchange pathways have been marked in panels (b)–(d). (e) Experimentally observed and refined powder XRD pattern of BNRIO.

lattice in the $a - b$ plane [Fig. 1(d)]. Depending on the choice of the M , these materials show signatures of dimerlike phase, ferromagnetlike features, and a quantum spin-orbital liquid state [10,11,22]. Surprisingly, the replacement of nonmagnetic Zn^{2+} by magnetic Ni^{2+} does not result in either spin freezing or spin ordering down to 100 mK despite appreciable magnetic interactions between Ir and Ni sublattices in $\text{Ba}_3\text{NiIr}_2\text{O}_9$ (BNIO) [12]. On the other hand, $\text{Ba}_3\text{NiRu}_2\text{O}_9$ (BNRO), where no effect of SOC is expected due to the half-filled t_{2g} states for Ru^{5+} , undergoes a long-range antiferromagnetic transition involving both Ni and Ru sublattices around 110 K [23]. Interestingly, mixed triple perovskite $\text{Ba}_3\text{NiRuIrO}_9$ (BNRIO) can be also stabilized in $P6_3/mmc$ structures [24], similar to BNIO and BNRO. However, very

little about its electronic and magnetic properties is known, which makes it a potential candidate for detailed experimental and theoretical investigations.

In this work, we investigate $\text{Ba}_3\text{NiRuIrO}_9$ using x-ray absorption spectroscopy (XAS), dc and ac magnetometry, neutron powder diffraction (NPD), and density functional theory + Hubbard U (DFT+ U) calculations. XAS measurements at the Ni $L_{3,2}$ edge confirm the desired +2 oxidation state. Branching ratio analysis of Ir $L_{3,2}$ -edge XAS [25] demonstrates a reduction of SOC in BNRIO compared to BNIO. Our dc and ac magnetic susceptibility measurements have found evidence of short-ranged magnetic correlation below 170 K. Neutron diffraction measurements have further demonstrated the development of a long-range antiferromagnetic ordering below 80 K with ferromagnetic (FM) interactions between Ni and Ru/Ir and antiferromagnetic (AFM) interactions between Ru and Ir sites. The DFT+ U calculations in the presence of spin-orbit coupling also find the same magnetic configurations as the lowest energy configuration, complementing our findings from NPD.

II. METHODS

BNRIO is synthesized in polycrystalline form starting from the powders of BaCO_3 , NiO , RuO_2 , and Ir (all purchased from Sigma-Aldrich) in the stoichiometric ratio. RuO_2 powder was preheated at 900 °C before taking weight. All the powders were grounded well and first heated at 900 °C for calcination. The mixture was heated for 12 h at 1150 °C under an oxygen atmosphere within a tube furnace after thorough grinding. This step was repeated nine times to get a phase pure sample and the powder x-ray diffraction (XRD) pattern was recorded at various stages of this process. Powder XRD was carried out using a laboratory-based Rigaku Smartlab diffractometer, having a $\text{Cu } K_\alpha$ source. Temperature-dependent XRD measurements were also carried out in the Indian beamline (BL-18B) at the Photon Factory, KEK, Japan. The diffraction pattern of the final phase was refined by the Rietveld method using FULLPROF [26]. XAS across the Ni $L_{3,2}$ edge was recorded in bulk sensitive total fluorescence yield mode at the 4-ID-C beamline of Advanced Photon Source, USA. The XAS spectra for Ir $L_{3,2}$ edges were collected using transmission mode at the EXAFS beamline of Elettra Trieste, Italy. A Quantum Design (QD) MPMS SQUID magnetometer was used for magnetic susceptibility measurements. Neutron powder diffraction at 300 K and 15 K were carried out using the multiposition-sensitive detector-based focusing crystal diffractometer set up by UGC-DAE Consortium for Scientific Research (UGC-DAE CSR) Mumbai Centre at the National Facility for Neutron Beam Research (NFNBR), Dhruva reactor, Mumbai (India). Temperature-dependent time of flight (TOF) neutron powder diffraction measurements were further carried out at the WISH beamline [27] of the ISIS neutron and muon source, Rutherford Appleton Laboratory, UK. For the NPD experiment, approximately 1 g of the sample was packed in a thin vanadium can and loaded into the He-flow cryostat. Data obtained at the WISH beamline have been shown in the main text. All the data were collected during warming from the base temperature and the data normalization has been performed using Mantid [28].

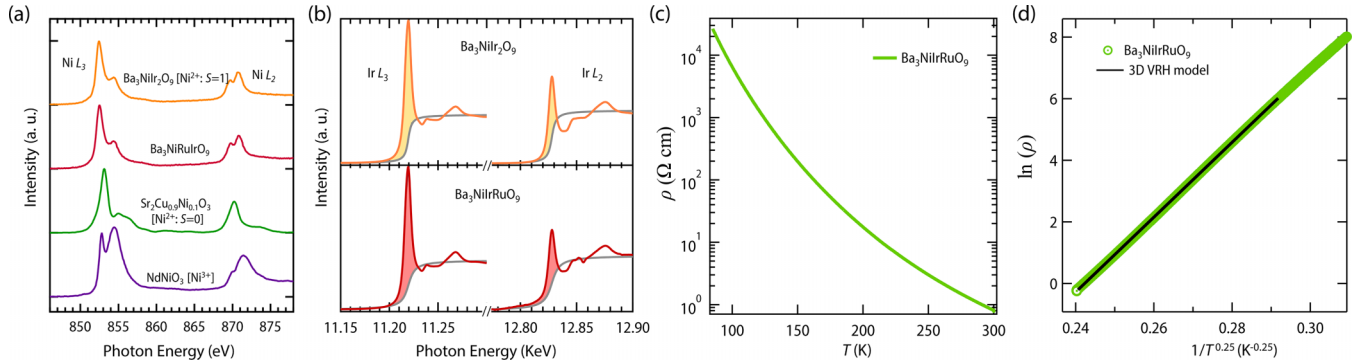


FIG. 2. (a) Ni $L_{3,2}$ -edge XAS spectra for $\text{Ba}_3\text{NiIrRuO}_9$, $\text{Ba}_3\text{NiIr}_2\text{O}_9$ (Ni^{2+} : $S=1$) [12], $\text{Sr}_2\text{Cu}_{0.9}\text{Ni}_{0.1}\text{O}_3$ (Ni^{2+} : $S=0$) [42], and NdNiO_3 (Ni^{3+}) [43]. (b) Ir $L_{3,2}$ -edge XAS for $\text{Ba}_3\text{NiIr}_2\text{O}_9$ (top) and $\text{Ba}_3\text{NiIrRuO}_9$ (bottom) showing the white line features. (c) ρ as a function of T . The fitting of ρ by the three-dimensional VRH model has been shown in panel (d).

Electronic structure calculations have been carried out within the framework of density functional theory (DFT) using the full potential linearized augmented plane wave (FP-LAPW) method as implemented in WIEN2K code [29]. Exchange and correlation effects are treated within the LSDA + U (local spin density approximation + Hubbard U) approach, where the strong electronic correlation effects are accounted for by including an orbital-dependent static U term in the DFT Hamiltonian. The value of U for Ni, Ru, and Ir d states are chosen as 6 eV, 2.5 eV, and 2.0 eV, respectively, following Refs. [12,30–32]. The effect of SOC on valence states has been included in an accurate second-variational method using scalar relativistic wave functions. To obtain well-converged Kohn-Sham eigenvalues, wave functions in the interstitial region are expanded in terms of plane waves with a cutoff $R_{MT}k_{\max} = 7$, where R_{MT} is the radius of the smallest atomic sphere and k_{\max} is the magnitude of the largest k vector.

For calculating the intersite magnetic interactions, we have also carried out LSDA + U + SOC calculations for the lowest energy state using the full-potential linear muffin-tin orbital (FP-LMTO) method [33,34] as implemented in the software package RSPT [35]. After obtaining the desired convergence, the magnetic force theorem [36,37] has been utilized to extract the effective intersite magnetic-interaction parameters. A detailed discussion of the implementation of the magnetic force theorem in RSPT is provided in Ref. [38].

III. RESULTS AND DISCUSSIONS

The powder XRD pattern of BNRIO, recorded at room temperature [see Fig. 1(e)], has been accurately indexed and refined using a $6H$ -type hexagonal crystal structure with space group (number 194) $P6_3/mmc$ with lattice constants $a = b = 5.74(5)$ Å and $c = 14.16(5)$ Å. The Ni and Ru/Ir are found to be present at the corner-shared ($2a$ site) and face-shared ($4f$ site) octahedral units, respectively, without intermixing. The structural parameters obtained from the refinement have been listed in the Supplemental Material (SM) [39]. We also note that refinement using a lower symmetry $P6_3mc$ space group (number 186), which allows ordered arrangements of Ru and Ir within the face-shared dimer unit [40], did not provide any improvement to the refinement results. The intradimer distance is ~ 2.71 Å, smaller than the Ir-Ir separation

(~ 2.76 Å) found in the BNIO compound, which would facilitate a larger electronic hopping. We have also performed temperature-dependent XRD down to 15 K and the structural symmetry remains unchanged.

In BNIO, Ni and Ir have an oxidation state of +2 and +5, respectively [12]. We have performed XAS measurements at Ni and Ir $L_{3,2}$ edges of BNRIO to examine whether Ru doping leads to any changes. For a $3d$ transition metal, the $2p^63d^n \rightarrow 2p^53d^{n+1}$ transition is probed using soft x ray, where the spectral line shape of $L_{3,2}$ edges are susceptible to the valency, spin character of the initial state, and crystal field environment of the system [41]. In Fig. 2(a), Ni $L_{3,2}$ -edge XAS for BNRIO has been shown along with the spectrum of Ni^{2+} with $S=1$ (BNIO) [12], Ni^{2+} with $S=0$ (Ni doped Sr_2CuO_3) [42], and Ni^{3+} (NdNiO_3) [43]. The line positions and shapes establish that the Ni in BNRIO is in a +2 oxidation state with a high spin ($S=1$) configuration.

Figure 2(b) shows the L_3 and L_2 edge XAS of Ir ($2p^65d^n \rightarrow 2p^55d^{n+1}$ transition) for BNIO and BNRIO, where no shift in white line peak positions validates the same +5 oxidation state of Ir in both compounds. The branching ratio (BR), which is the ratio of integrated intensities of the white line feature obtained at the L_3 to L_2 absorption edge (i.e., I_{L_3}/I_{L_2}) [25,44,45], is found to be 5.77 and 4.02 for BNIO and BNRIO, respectively. The BR for BNIO is also found to be very similar to the value (5.8) reported for Ir^{5+} containing $\text{Sr}_3\text{CaIr}_2\text{O}_9$ [46]. For both BNIO and BNRIO, the BR is larger than the statistical BR of 2, signifying a strong coupling between the local orbital and spin moments. Furthermore, this BR is directly linked to the ground state expectation value of the spin-orbit coupling $\mathbf{L} \cdot \mathbf{S}$ [47] as

$$BR = \frac{2 + \mathbf{r}}{1 - \mathbf{r}}, \quad \text{with} \quad \mathbf{r} = \frac{\langle \mathbf{L} \cdot \mathbf{S} \rangle}{\langle n_h \rangle}, \quad (1)$$

where $\langle n_h \rangle$ is the number of $5d$ holes. Considering $n_h = 6$, we obtain $\langle \mathbf{L} \cdot \mathbf{S} \rangle$ values of $3.3\hbar^2$ and $2.4\hbar^2$ for BNIO and BNRIO, respectively. We attribute the lowering of $\langle \mathbf{L} \cdot \mathbf{S} \rangle$ in BNRIO to the increased hopping strength [48].

According to the results obtained from XAS measurement, the RuIrO_9 face-shared dimer unit has seven d electrons. The band theory would predict a metallic phase without considering any correlation and SOC in such a case. Our temperature-dependent electrical resistivity measurement has

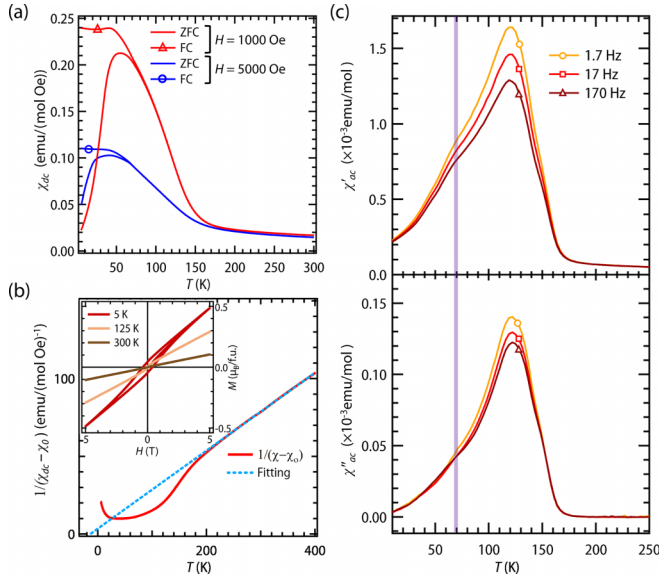


FIG. 3. (a) FC and ZFC χ_{dc} as a function of T , recorded in the presence of 1000 Oe and 5000 Oe. (b) Curie-Weiss analysis of χ_{dc} with 5000 Oe data. Inset: M - H curve recorded at several fixed temperatures. (c) Real (χ'_{ac}) and imaginary (χ''_{ac}) parts of ac susceptibility for $\text{Ba}_3\text{NiRuIrO}_9$.

found the insulating behavior of the compound [Fig. 2(c)], which can be further fitted with the variable range hopping model in three dimensions [Fig. 2(d)]. Our spin-polarized DFT+ U calculations, discussed later in the manuscript, further find that the insulating state can be obtained only after incorporating SOC, further demonstrating that SOC is a deterministic energy scale in this material.

We next focus on the magnetic structure. Figure 3(a) shows the zero-field-cooled (ZFC) and field-cooled (FC) dc susceptibility (χ_{dc}) as a function of temperature (T), measured in warming cycles from 5 K to 300 K (5 K to 400 K) in the presence of applied magnetic field of 1000 Oe (5000 Oe). Both FC and ZFC- χ_{dc} show strong field dependence below 170 K, signifying the development of magnetic correlations. In the measurement with an applied field of 1000 Oe, a bifurcation between the FC and ZFC curve is observed below 70 K. ZFC χ_{dc} further shows a broad peak around 50 K, whereas the FC tends to saturate at lower temperatures. The low-temperature saturation in FC susceptibility is further prominent in measurement with a 5000 Oe field. All of these observations suggest the presence of competing ferromagnetic (FM) and antiferromagnetic (AFM) interactions [49]. By fitting the high-temperature part of χ_{dc} [Fig. 3(b)] using a modified Curie-Weiss law of the form $\chi_{dc} = \chi_o + C_W/(T - \theta_{CW})$ (here χ_o accounts for a Van Vleck paramagnetic susceptibility), we have obtained the Curie-Weiss temperature (θ_{CW}) = -14 K. The much smaller magnitude of $|\theta_{CW}|$ compared to the temperature scale where the magnetic correlation develops (~ 170 K) further supports the competition between FM and AFM interactions and the negative sign of θ_{CW} implies the net magnetic interaction is AFM type. The effective magnetic moment ($\mu_{\text{eff}} = \sqrt{8C_W}$) is $5.65 \mu_B/\text{f.u.}$ (f.u. = formula unit). Considering $g \sim 2.5$ for Ni^{2+} with high spin configuration [50], the effective moment for each face-shared

octahedral unit ($= \sqrt{\mu_{\text{eff}}^2 - \mu_{\text{Ni}^{2+}}^2}$) is calculated to be $4.4 \mu_B$, which cannot be generated only by either Ru^{5+} or Ir^{5+} . The M vs H curve measured at 5 K shows significant hysteresis [inset of Fig. 3(b)] without any signature of saturation within the field of our measurement, signifying the presence of considerable ferromagnetic interaction between the spins. There is no irreversibility between the magnetization measured during sweeping the field from +5 T to -5 T and the reverse way for measurement at 125 K and 300 K.

Apart from dc susceptibility measurements, ac susceptibility has also been measured at three different frequencies: 1.7 Hz, 17 Hz, and 170 Hz, to get details of the spin dynamics happening in the system. The real (χ'_{ac}) and imaginary (χ''_{ac}) parts of ac susceptibility rise below 170 K [Fig. 3(c)], similar to χ_{dc} , and show a broad peak around 122 K. The magnitudes of χ'_{ac} and χ''_{ac} become a function of the drive frequency below 150 K and the peak position shows a very small shift (~ 1 K; see $d\chi'_{ac}/dT$ vs T plot, Fig. S1 in SM [39]). The temperature onsets of χ'_{ac} and χ''_{ac} below 170 K are not sharp, yet do not show a large frequency dependence. The $\chi'_{ac}(T, f)$ and $\chi''_{ac}(T, f)$ curves in Fig. 3(c) are reminiscent of those observed in systems with short-ranged magnetic order [51]. This suggests some magnetic correlation developing below 170 K in this system, in agreement with the dc magnetization data. Furthermore, the $\chi'_{ac}(T, f)$ and $\chi''_{ac}(T, f)$ curves exhibit another anomaly near 70 K, which seems to correspond to the onset of magnetic irreversibility in the ZFC/FC curves.

To investigate the presence of any long-range magnetic ordering, we have performed neutron powder diffraction (NPD) starting from 1.5 K to room temperature. The room temperature NPD can be satisfactorily refined using space-group $P6_3/mmc$ along with a less than 1% NiO impurity phase [lower panel of Fig. 4(a)], in line with the XRD refinements. A closer look at the scans at 1.5 K reveals an additional peak appearing at $d = 2.82 \text{ \AA}$, as shown in Fig. 4(b). This peak has an index of $(2\bar{1}1)$, which is forbidden in the space group of $P6_3/mmc$. Some extra intensity related to magnetic origin has also been observed at the $d = 3.42 \text{ \AA}$, i.e., (103) nuclear Bragg peaks. The temperature variation of intensity of the peak at $d = 2.82 \text{ \AA}$, computed by integrating the area under the curve, is shown in Fig. 4(c), which reveals that the peak decreases with increasing temperature and disappears between 70 and 80 K. This is the same temperature range where the bifurcation of ZFC and FC is found in dc susceptibility and a small feature is observed in ac susceptibility measurements. The NPD pattern, recorded at 1.5 K, can be refined by adding an additional magnetic phase with a magnetic propagation vector $k = (000)$ and a magnetic unit cell similar to the crystallographic unit cell. The refined spin configuration is shown in Fig. 4(d) and the refinement results are shown in the Table S2, of SM [39]. Here, the Ir/Ru spins align antiferromagnetically within the dimers and interact ferromagnetically with the Ni. Although the difference in the magnetic moment of the Ir and Ru gives a net ferrimagnetic interaction within a dimer, individual Ir/Ru magnetic moments cannot be extracted from NPD measurements due to the disordered arrangement. We have found an average moment of $0.5(1) \mu_B$ for Ir/Ru sublattice and $1.48(7) \mu_B$ for Ni sublattices. The same spin configuration has also been found by the refinement

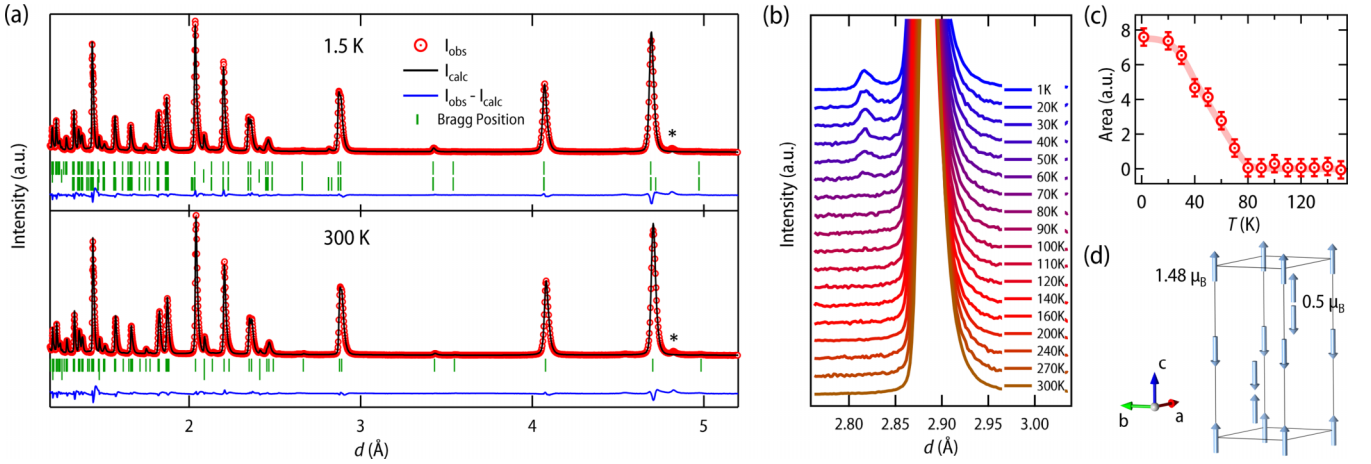


FIG. 4. (a) Experimental (red) and refined (black) neutron powder diffraction patterns of $\text{Ba}_3\text{NiRuIrO}_9$ at 1.5 K and 300 K. There is an unidentified peak around $d = 4.82 \text{ \AA}$ (marked by an asterisk), present at all temperatures. (b) NPD patterns recorded at different temperatures have been shown around $d = 2.9 \text{ \AA}$ to emphasize the appearance of an additional magnetic peak at $d = 2.82 \text{ \AA}$. Different data have been vertically shifted along the y axis by different amounts for visual clarity. (c) The area under the magnetic peak at $d = 2.82 \text{ \AA}$ has been plotted as a function of T to determine the magnetic transition temperature. (d) Magnetic unit cell obtained by refinement of NPD at 1.5 K.

of the NPD pattern at 15 K, recorded at the UGC-DAE CSR beamline (see Fig. S2, the SM [39]).

Our experimental observations of a long-range magnetic ordering have been further complemented by first-principles DFT+ U calculations. Since both Ru and Ir are located in the same crystallographic site, we started our theoretical analysis by finding out the most stable arrangement of Ir and Ru ions in the unit cell. We have found that the configuration containing each dimer with one Ru and one Ir is lower in energy by 15 meV than the unit cell containing Ru_2O_9 and Ir_2O_9 dimers. We have further investigated the magnetism considering this lower energy atomic arrangement using the LSDA + U approach including SOC. Considering the possibilities of ferromagnetic (FM) and antiferromagnetic (AFM) interactions between Ru and Ir within a dimer and between Ni and Ru/Ir, we have investigated four different magnetic configurations [Fig. 5(a)]. The total energies, spin, and orbital moments, obtained from LSDA + U + SOC calculations (with $U = 2.0 \text{ eV}$ on Ir), for these magnetic states are tabulated in Table I. These results provided a few important insights about the nature of magnetism. First, the lowest energy magnetic configuration (AFM1) consists of a strong antiferromagnetic dimer, while the Ni-Ru and Ni-Ir magnetic interactions are ferromagnetic. This agrees with the experimentally observed magnetic structure from the NPD

measurement. We also note here that the AFM1 state remains the lowest in energy even with $U = 1.5 \text{ eV}$, indicating that the nature of couplings is robust with respect to the choice of U when it is chosen within the reasonable range [31].

Furthermore, we have found that the orbital moment for Ir is almost half of its spin moment. Meanwhile, the orbital moment for Ru ions is negligible, as expected, due to its half-filled t_{2g} orbitals where the orbital moment is quenched. The lower value of spin moment for Ru compared to the naive atomic consideration ($3 \mu_B$ for d^3 consideration) is related to the strong Ru-O hybridization effect [52]. The magnetic moments of Ni and the average moment of Ru/Ir are also close to the values obtained from the refinement of the NPD pattern at 1.5 K.

Since SOC is found to be significantly strong, we mapped the computed energies from LSDA + U + SOC calculations onto a generalized Heisenberg model as given below:

$$H = - \sum_{i \neq j} e_i^\alpha J_{ij}^{\alpha\beta} e_j^\beta, \quad \alpha, \beta = x, y, z. \quad (2)$$

Here, the magnetic exchange parameter $J_{ij}^{\alpha\beta}$ is a rank-2 tensor for the fully relativistic case and is extracted by the Korringa-Kohn-Rostoker (KKR) Green's-function method [53,54]. This method has been successfully adopted for various

TABLE I. LSDA + U + SOC calculations for obtaining the lowest energy magnetic configuration. The moments, written within parentheses, denote orbital moments.

Spin config.	Interaction type		Energy (meV/u.c.)	Magnetic moment (μ_B)		
	Ru-Ir	Ni-Ru/Ir		Ni	Ru	Ir
FM	FM	FM	0.00	1.72 (0.22)	1.72 (0.07)	0.42 (0.17)
FM1	FM	AFM	71.67	-1.70 (0.20)	1.60 (0.08)	0.60 (0.27)
AFM1	AFM	FM	-826.98	1.75 (0.27)	1.72 (0.08)	0.57 (0.27)
AFM2	AFM	AFM	194.69	1.69 (0.22)	1.62 (0.09)	0.23 (0.10)

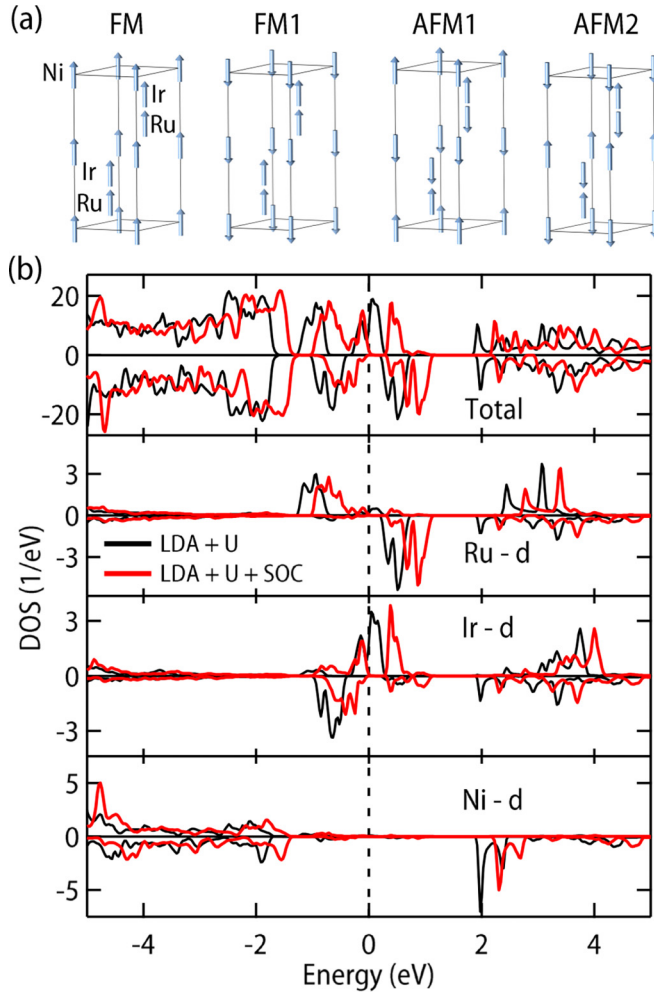


FIG. 5. (a) Various possible magnetic states considered for DFT calculation. (b) Total and partial density of states as obtained from LSDA + U (black) and LSDA + U + SOC (red) calculations for AFM1 configuration.

systems that possess significant spin-orbit coupling [55,56]. In the $J_{ij}^{\alpha\beta}$ matrix, diagonal terms are related to isotropic Heisenberg exchange, while off-diagonal components provide Dzyaloshinski-Moriya (DM) interactions and symmetric anisotropic exchange. In this work, we have reported only the isotropic Heisenberg intersite exchange interaction as displayed in Table II. Here, it can be seen that Ir and Ru in the dimer structure are strongly coupled in an AFM manner, while

TABLE II. Intersite exchange coupling strength of BNRIO obtained from LSDA + U + SOC calculations. -ve (+ve) sign of J refers to antiferromagnetic (ferromagnetic) type interaction.

Interaction	No. of neighbors	Bond	J_{ij} (meV)
J_1	1	Ir-Ru	-20.14
J_2	3	Ir-Ni	3.36
J_3	3	Ru-Ni	4.81
J_4	6	Ir-Ir	-0.23
		Ru-Ru	-0.13

other couplings are very weak in comparison. The Ni-Ru and Ni-Ir interactions are also significantly large and are FM in nature. Since Ir-Ir and Ru-Ru interactions in the hexagonal a - b plane [denoted by J_4 in Fig. 1(d)] are antiferromagnetic, they can induce magnetic frustration. However, due to their small values compared to the J_1 and J_2 [for exchange paths, see Figs. 1(b)–1(d)], a long-range ordering appears in this material.

In order to investigate if our conclusion about long range ordering is structure dependent or not, we also computed interatomic magnetic couplings for a structure which consists of homonuclear dimers (Ir-Ir and Ru-Ru dimers as shown in Fig. S3 of the SM [39]). We found that the strength and nature of the couplings (J_1 to J_4) are very similar (see Table S4 in the SM [39]) to those reported above. Hence we can conclude that long-range ordering will be established even if homonuclear dimers are formed in our synthesized material.

We have also considered magnetocrystalline anisotropy (MAE) energy in this material due to the presence of large SOC on Ir [57–59]. We have computed MAE by computing the total energy for different spin-quantization axes. We find that the crystallographic c axis comes out to be the easy axis of magnetization with a large MAE value of -48.26 meV. This is also consistent with the spin arrangements obtained from NPD [Fig. 4(d)].

Finally, we calculated the electronic structure for the AFM1 state, which was the lowest in energy. The total density of states (DOS) and atomic projected DOS are displayed in Fig. 5(b). From the total DOS, we observe that LSDA + U calculation gives finite spectral weight at the Fermi level, suggesting a metallic ground state. The experimentally observed insulating state is obtained only when the SOC is also included in our calculations. The computed band gap comes out to be 0.37 eV. Further to understand the role of various atomic orbitals, we have computed orbital projected DOS for all various ions separately. In the PDOS of Ni- d states, a gap is observed between minority d states in both LSDA + U and LSDA + U + SOC results. The spectral function is consistent with the nominal +2 charge state of Ni ($3d^8$), where the majority channel is fully occupied and the gap is formed between minority t_{2g} and e_g states. For Ru- d PDOS, a t_{2g} -majority channel is completely filled, while a t_{2g} -minority channel appears above the Fermi level. The Ru- e_g states of both spin channels are completely unoccupied, lying well above the Fermi level. Such arrangement of Ru- d states is consistent with nominal d^3 occupancy as discussed before. As expected, the orbital moment is almost fully quenched in half-filled orbitals, leading to a negligibly small effective SOC. Hence we do not observe any significant difference between LSDA + U and LSDA + U + SOC Ru- d spectral function. The overall shape of the spectral functions are found to be similar; however, a hybridization-driven linear shift is noticed. For PDOS of Ir- d , we observe that LSDA + U gives rise to a finite spectral weight of Ir- d at the Fermi level, resulting in the system's metallic behavior. On the inclusion of the SOC, Ir- t_{2g} states exhibit a major modification and a gap opens up. Thus we conclude that the SOC effect arising from Ir- d is responsible for the insulating ground state of this system. Hence our system belongs to a member of the spin-orbit driven Mott-Hubbard insulator [60].

IV. CONCLUSIONS

To summarize, our comprehensive investigation combining several experimental techniques along with DFT calculations demonstrates that $6H$ BNRIO is a spin-orbit driven Mott-Hubbard insulator and undergoes a long-range antiferromagnetic ordering below 80 K involving Ni, Ru, and Ir. While the in-plane antiferromagnetic interaction between Ir_2O_9 dimers was attributed as the reason behind the cooperative paramagnetic state of $\text{Ba}_3\text{NiIr}_2\text{O}_9$ [12], the strength of in-plane Ir-Ir and Ru-Ru antiferromagnetic interaction on a triangular lattice is much weaker compared to the leading magnetic interaction scale in $\text{Ba}_3\text{NiRuIrO}_9$, leading to a long-range magnetic ordering. A series of $\text{Ba}_3M\text{RuIrO}_9$ can be synthesized with M^{1+} , M^{2+} , and M^{3+} [24,61] and it will be interesting to understand the relation among magnetism, SOC strength, and electron filling within these materials.

ACKNOWLEDGMENTS

The authors acknowledge the XRD facilities at the Department of Physics, IISc Bangalore. S.M. acknowl-

edges funding support from a SERB Core Research grant (Grant No. CRG/2022/001906). S.K.P. acknowledges funding support from a SERB Core Research grant (Grant No. CRG/2023/003063). This research used resources from the Advanced Photon Source, a U.S. Department of Energy Office of Science User Facility operated by Argonne National Laboratory under Contract No. DE-AC02-06CH11357. For experiments at the ISIS Neutron and Muon Source (beamtime allocation RB2368017), the authors thank the Department of Science and Technology, India (Grant No. SR/NM/Z-07/2015) for the access to the experimental facility and financial support to carry out the experiment and Jawaharlal Nehru Centre for Advanced Scientific Research (JNCASR) for managing the project. The authors thank the Department of Science and Technology, India for the financial support and Saha Institute of Nuclear Physics and Jawaharlal Nehru Centre for Advanced Scientific Research, India, for facilitating the experiments at the Indian Beamline, Photon Factory, KEK, Japan. The authors also thank Elettra Sincrotrone Trieste for providing access to its synchrotron radiation facilities at the XAFS beamline. D.D.K. acknowledges financial support from the EPSRC, UK, through Grant No. /W00562X/1.

-
- [1] M. Imada, A. Fujimori, and Y. Tokura, *Rev. Mod. Phys.* **70**, 1039 (1998).
- [2] W. Witzak-Krempa, G. Chen, Y. B. Kim, and L. Balents, *Condens. Matter Phys.* **5**, 57 (2013).
- [3] R. Schaffer, E. K.-H. Lee, B.-J. Yang, and Y. B. Kim, *Rep. Prog. Phys.* **79**, 094504 (2016).
- [4] A. J. Browne, A. Krajewska, and A. S. Gibbs, *J. Mater. Chem. C* **9**, 11640 (2021).
- [5] T. Takayama, J. Chaloupka, A. Smerald, G. Khaliullin, and H. Takagi, *J. Phys. Soc. Jpn.* **90**, 062001 (2021).
- [6] G. Cao and P. Schlottmann, *Rep. Prog. Phys.* **81**, 042502 (2018).
- [7] D. I. Khomskii and S. V. Streltsov, *Chem. Rev.* **121**, 2992 (2021).
- [8] G. Khaliullin, *Phys. Rev. Lett.* **111**, 197201 (2013).
- [9] S. Guo, K. M. Powderly, and R. J. Cava, *Dalton Trans.* **49**, 12018 (2020).
- [10] A. Nag, S. Middey, S. Bhowal, S. K. Panda, R. Mathieu, J. C. Orain, F. Bert, P. Mendels, P. G. Freeman, M. Mansson, H. M. Ronnow, M. Telling, P. K. Biswas, D. Sheptyakov, S. D. Kaushik, V. Siruguri, C. Meneghini, D. D. Sarma, I. Dasgupta, and S. Ray, *Phys. Rev. Lett.* **116**, 097205 (2016).
- [11] A. Nag, S. Bhowal, F. Bert, A. D. Hillier, M. Itoh, I. Carluomagno, C. Meneghini, T. Sarkar, R. Mathieu, I. Dasgupta, and S. Ray, *Phys. Rev. B* **97**, 064408 (2018).
- [12] S. Kumar, S. K. Panda, M. M. Patidar, S. K. Ojha, P. Mandal, G. Das, J. W. Freeland, V. Ganesan, P. J. Baker, and S. Middey, *Phys. Rev. B* **103**, 184405 (2021).
- [13] G. Cao, T. F. Qi, L. Li, J. Terzic, S. J. Yuan, L. E. DeLong, G. Murthy, and R. K. Kaul, *Phys. Rev. Lett.* **112**, 056402 (2014).
- [14] M. A. Laguna-Marco, P. Kayser, J. A. Alonso, M. J. Martínez-Lope, M. van Veenendaal, Y. Choi, and D. Haskel, *Phys. Rev. B* **91**, 214433 (2015).
- [15] T. Dey, A. Maljuk, D. V. Efremov, O. Kataeva, S. Gass, C. G. F. Blum, F. Steckel, D. Gruner, T. Ritschel, A. U. B. Wolter, J. Geck, C. Hess, K. Koepf, J. van den Brink, S. Wurmehl, and B. Büchner, *Phys. Rev. B* **93**, 014434 (2016).
- [16] M. Bremholm, S. E. Dutton, P. W. Stephens, and R. J. Cava, *J. Solid State Chem.* **184**, 601 (2011).
- [17] J. Dai, Y. Yin, X. Wang, X. Shen, Z. Liu, X. Ye, J. Cheng, C. Jin, G. Zhou, Z. Hu, S. Weng, X. Wan, and Y. Long, *Phys. Rev. B* **97**, 085103 (2018).
- [18] W. K. Zhu, M. Wang, B. Seradjeh, F. Yang, and S. X. Zhang, *Phys. Rev. B* **90**, 054419 (2014).
- [19] S. Bhowal and I. Dasgupta, *J. Phys.: Condens. Matter* **33**, 453001 (2021).
- [20] A. Nag, S. Bhowal, M. M. Sala, A. Efimenko, I. Dasgupta, and S. Ray, *Phys. Rev. Lett.* **123**, 017201 (2019).
- [21] Q. Chen, C. Svoboda, Q. Zheng, B. C. Sales, D. G. Mandrus, H. D. Zhou, J.-S. Zhou, D. McComb, M. Randeria, N. Trivedi, and J.-Q. Yan, *Phys. Rev. B* **96**, 144423 (2017).
- [22] M. S. Khan, A. Bandyopadhyay, A. Nag, V. Kumar, A. V. Mahajan, and S. Ray, *Phys. Rev. B* **100**, 064423 (2019).
- [23] J. Rijssenbeek, Q. Huang, R. Erwin, H. Zandbergen, and R. Cava, *J. Solid State Chem.* **146**, 65 (1999).
- [24] M. W. Lufaso and H.-C. zur Loye, *Inorg. Chem.* **44**, 9154 (2005).
- [25] D. Haskel, G. Fabbris, M. Zhernenkov, P. P. Kong, C. Q. Jin, G. Cao, and M. van Veenendaal, *Phys. Rev. Lett.* **109**, 027204 (2012).
- [26] J. Rodríguez-Carvajal, *Phys. B: Condens. Matter* **192**, 55 (1993).
- [27] D. Duxbury, D. Khalyavin, P. Manuel, D. Raspino, N. Rhodes, E. Schooneveld, and E. Spill, *J. Instrum.* **9**, C12008 (2014).
- [28] O. Arnold, J. Bilheux, J. Borreguero, A. Buts, S. Campbell, L. Chapon, M. Doucet, N. Draper, R. F. Leal, M. Gigg, V. Lynch, A. Markvardsen, D. Mikkelsen, R. Mikkelsen, R. Miller,

- K. Palmen, P. Parker, G. Passos, T. Perring, P. Peterson *et al.*, *Nucl. Instrum. Methods Phys. Res., A* **764**, 156 (2014).
- [29] K. Schwarz and P. Blaha, *Comput. Mater. Sci.* **28**, 259 (2003).
- [30] J. Mravlje, M. Aichhorn, T. Miyake, K. Haule, G. Kotliar, and A. Georges, *Phys. Rev. Lett.* **106**, 096401 (2011).
- [31] X. Wan, A. M. Turner, A. Vishwanath, and S. Y. Savrasov, *Phys. Rev. B* **83**, 205101 (2011).
- [32] S. K. Panda, S. Bhowal, A. Delin, O. Eriksson, and I. Dasgupta, *Phys. Rev. B* **89**, 155102 (2014).
- [33] O. K. Andersen, *Phys. Rev. B* **12**, 3060 (1975).
- [34] J. M. Wills and B. R. Cooper, *Phys. Rev. B* **36**, 3809 (1987).
- [35] J. M. Wills, O. Eriksson, M. Alouani, and D. L. Price, Full-potential LMTO total energy and force calculations, in *Electronic Structure and Physical Properties of Solids*, edited by H. Dreyssé, Lecture Notes in Physics, Vol. 535 (Springer, Berlin, 2000), pp. 148–167.
- [36] A. I. Liechtenstein, M. Katsnelson, V. Antropov, and V. Gubanov, *J. Magn. Magn. Mater.* **67**, 65 (1987).
- [37] M. I. Katsnelson and A. I. Liechtenstein, *Phys. Rev. B* **61**, 8906 (2000).
- [38] Y. O. Kvashnin, O. Grånäs, I. Di Marco, M. I. Katsnelson, A. I. Liechtenstein, and O. Eriksson, *Phys. Rev. B* **91**, 125133 (2015).
- [39] See Supplemental Material at <http://link.aps.org/supplemental/10.1103/PhysRevB.110.024407> for structural information, ac susceptibility, magnetic unit cell information, and magnetic exchange coupling strength for homonuclear dimer setup.
- [40] J. G. Cheng, G. Li, L. Balicas, J. S. Zhou, J. B. Goodenough, C. Xu, and H. D. Zhou, *Phys. Rev. Lett.* **107**, 197204 (2011).
- [41] J. Stöhr and H. C. Siegmann, X-rays and magnetism: Spectroscopy and microscopy, in *Magnetism From Fundamentals to Nanoscale Dynamic* (Springer, Berlin, Heidelberg, 2006), pp. 431–476.
- [42] P. Mandal, R. K. Patel, D. Rout, R. Banerjee, R. Bag, K. Karmakar, A. Narayan, J. W. Freeland, S. Singh, and S. Middey, *Phys. Rev. B* **103**, L060504 (2021).
- [43] J. W. Freeland, M. van Veenendaal, and J. Chakhalian, *J. Electron Spectrosc. Relat. Phenom.* **208**, 56 (2016), Special Issue: Electronic structure and function from state-of-the-art spectroscopy and theory.
- [44] G. van der Laan and B. T. Thole, *Phys. Rev. Lett.* **60**, 1977 (1988).
- [45] B. T. Thole and G. van der Laan, *Phys. Rev. B* **38**, 3158 (1988).
- [46] A. de la Torre, B. Zager, J. R. Chamorro, M. H. Upton, G. Fabbris, D. Haskel, D. Casa, T. M. McQueen, and K. W. Plumb, *Phys. Rev. Mater.* **6**, 084406 (2022).
- [47] B. T. Thole and G. van der Laan, *Phys. Rev. A* **38**, 1943 (1988).
- [48] M. Rossi, M. Retegan, C. Giacobbe, R. Fumagalli, A. Efimenko, T. Kulka, K. Wohlfeld, A. I. Gubanov, and M. Moretti Sala, *Phys. Rev. B* **95**, 235161 (2017).
- [49] M. Halder, S. M. Yusuf, A. Kumar, A. K. Nigam, and L. Keller, *Phys. Rev. B* **84**, 094435 (2011).
- [50] R. L. Carlin, *Magnetochemistry* (Springer Science & Business Media, New York, 2012).
- [51] R. Padam, T. Sarkar, R. Mathieu, S. Thota, and D. Pal, *J. Appl. Phys.* **122**, 073908 (2017).
- [52] S. V. Streltsov, *Phys. Rev. B* **88**, 024429 (2013).
- [53] L. Udvardi, L. Szunyogh, K. Palotás, and P. Weinberger, *Phys. Rev. B* **68**, 104436 (2003).
- [54] H. Ebert and S. Mankovsky, *Phys. Rev. B* **79**, 045209 (2009).
- [55] V. Borisov, Y. O. Kvashnin, N. Ntallis, D. Thonig, P. Thunström, M. Pereiro, A. Bergman, E. Sjöqvist, A. Delin, L. Nordström, and O. Eriksson, *Phys. Rev. B* **103**, 174422 (2021).
- [56] V. Borisov, N. Salehi, M. Pereiro, A. Delin, and O. Eriksson, *npj Comput. Mater.* **10**, 53 (2024).
- [57] J. H. van Vleck, *Phys. Rev.* **52**, 1178 (1937).
- [58] P. C. Rout and U. Schwingenschlogl, *Nano Lett.* **21**, 6807 (2021).
- [59] X. Liang, X. Wu, J. Hu, J. Zhao, and X. C. Zeng, *Commun. Phys.* **1**, 74 (2018).
- [60] B. J. Kim, H. Jin, S. J. Moon, J.-Y. Kim, B.-G. Park, C. S. Leem, J. Yu, T. W. Noh, C. Kim, S.-J. Oh, J.-H. Park, V. Durairaj, G. Cao, and E. Rotenberg, *Phys. Rev. Lett.* **101**, 076402 (2008).
- [61] M. W. Lufaso and H.-C. zur Loye, *Inorg. Chem.* **44**, 9143 (2005).